Fluorescence tomography in turbid media based on acousto-optic modulation imaging

Masaki Kobayashi,[a] Takashi Mizumoto, Yukihiro Shibuya, and Masaru Enomoto
Department of Electronics, Tohoku Institute of Technology, Sendai 982-8577, Japan

Motohiro Takeda
Department of Bioengineering and Robotics, Graduate School of Engineering, Tohoku University, Sendai 980-8579, Japan

(Received 4 June 2006; accepted 7 September 2006; published online 30 October 2006)

The authors present a tomographic imaging technique of fluorescence in light-scattering media. Ultrasonic modulation of fluorescence based on the interaction between ultrasound and light is applied for imaging of a fluorescent material by scanning a focused sound field in which the light is modulated selectively. The on-axis sound-field characteristics that affect the light by modulating its amplitude (through variation of the refractive index and the scattering coefficient) were determined. That imaging technique is demonstrated using tissue phantoms that contain localized fluorescent regions in a dense scattering medium, suggesting the applicability of this technique for visualization of fluorescent probes in biological tissues. © *2006 American Institute of Physics*. [DOI: 10.1063/1.2364600]

Fluorescence imaging techniques that are employed in studies of life sciences have become increasingly important for assays of biological functions. Widely various fluorescent probes that are designed to be combined with target molecules, as well as a technique including genetic modification that produces fluorescent proteins, have been commonly used for visualization of dynamics of biofunctions that emerge in sites of vital phenomena in real time. Particularly, fluorescence techniques are the most powerful methods for visualization of cellular functions at the microscopic level. However, at the macroscopic level, light-scattering properties of biological tissues restrict the range of optical methods' applicability for investigations inside living bodies. A great deal of effort has been devoted to development of optical imaging in living bodies. Those efforts have improved characterization of the spatial distribution of optical properties. Time and frequency domain techniques[1] using near-infrared light characterizing diffuse light and coherent-gating[2,3] technique to extract the straightforward scattered light can facilitate tomographic imaging of biological tissues. Recently, *tagging* technique, which extracts optical information using some other physical energy, such as ultrasound, has garnered attention. Ultrasound tagging technique was demonstrated for extraction of optical absorption properties with assistance of less-scattered ultrasonic waves.[4–6] This technique is based on intensity modulation through fluctuation of speckles formed by multiply scattered coherent light in a varying sound-pressure field. By this principle, optical coherent properties are crucial for light modulation. However, displacement of scattering particles and variation of the refractive index that is induced by density distribution in a sound field might engender the intensity modulation of scattered light, even in incoherent light. In the tagging technique, which measures optical absorption, the incoherent modulation component is generally undetectable because the modulated component is too small in comparison to the unmodulated component of multiply scattered light.[7] However, for fluorescence measurement, the modulated component of fluorescence that is excited with modulated incoherent light is potentially detectable because of the spectral distinction between fluorescence and excitation wavelength under the appropriate optical arrangement of a detector for highly efficient light collection. In this letter, we demonstrate tomographic imaging of fluorescence in dense scattering media using tissue phantoms that involve small, localized fluorescent regions.

Figure 1 shows that the experimental setup comprises a continuous wave diode pumped solid state laser system (Verdi V-6; Coherent, Inc.) as a light source, an ultrasound transducer, and a photomultiplier tube (PMT) as a detector. The laser beam is reduced and collimated to 1 mm diameter and enters the water tank through a glass window. A focus-type ultrasonic transducer (38 mm focal length, 3 mm focal diameter, V314-SU; Olympus-NDT) that is driven by a 1 MHz continuous sinusoidal wave is incorporated into the

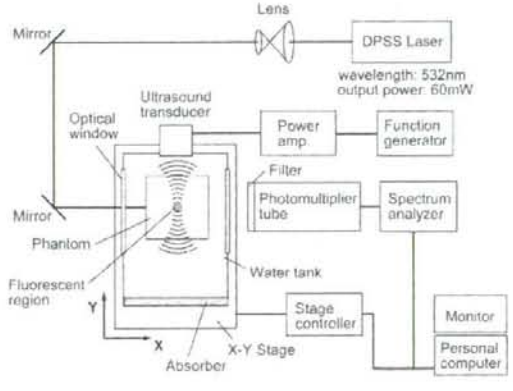

FIG. 1. (Color online) Schematic of the experimental setup. A water tank equipped with an ultrasound transducer is set on the *X-Y* autostage; a tissue phantom is fixed in place without touching the water tank.

[a]Electronic mail: masaki@tohtech.ac.jp

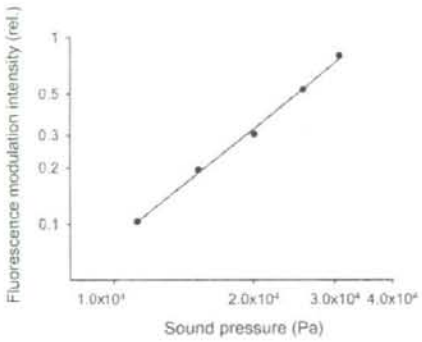

FIG. 2. Characteristics of fluorescence modulation intensity vs sound pressure in the ultrasound focus. Measurements were carried out while varying the excitation voltage applied to an ultrasound transducer focused on the fluorescent pigment in a tissue phantom.

side wall of the water tank, where the ultrasound beam traverses the incident axis of the laser beam. Sound pressure in the sound-field focus region was 4.1×10^4 Pa in water. The signal from the PMT is fed into a spectrum analyzer and the intensities of the resonant frequencies are detected using a narrow bandwidth (100 Hz). To obtain a two-dimensional tomographic image of fluorescence intensity through scanning of the ultrasound focus, a water tank equipped with a transducer is mounted on a two-axis translational stage and scanned in 500 μm steps along the X axis (parallel to the incident laser beam) and the Y axis (parallel to the ultrasound beam). It is controlled using a personal computer that is synchronized with a spectrum analyzer. A tissue phantom is suspended independently from the holder, which is located above the water tank; the phantom is immersed in the water without touching the water tank. The optical arrangement of the phantom and incident light remains unchanged during scanning of the ultrasound beam. The imaging experiments are conducted using a wavelength of 532 nm and an incident beam signal intensity of 60 mW.

The light modulation mechanism is inferred to be induced through density variation of the medium in the ultrasound field, which engenders changes of the refractive index and optical scattering coefficient. When fluorescent pigment is present in the sound field, the density variation of the medium engenders modulation of the photon density through deflection of light between two successive scattering events in the gradient of the refractive index, thereby causing fluorescence intensity modulation. Variation of the scattering coefficient also causes modulation of the fluorescence intensity.

Throughout the experiments, we used gel tissue phantoms of isotropic light-scattering media made of 5% agar (Inagel; Ina Food Industry Co. Ltd., Nagano, Japan) that were prepared through dilution of Intralipid (Intralipid 10%; Fresenius Kabi AG, Germany), which is a clinically useful fat emulsion that is often used for tissue phantom studies to elucidate light propagation in scattering media. The final volume concentration of Intralipid in the phantom was 40 ml/l in 5% agarose gel with the water-glycerin (20%) solution. The agarose gel was molded to $40 \times 40 \times 75$ mm^3. A fluorescent region in the phantom was formed by embedding a fluorescent material that contains fluorescent microspheres (530 nm absorption peak, 590 nm emission wavelength, fluoresbrite carboxylate microspheres, NYO; Polyscience, USA) molded with columnar agarose gel (5 mm long, 3 mm diameter). The reduced scattering coefficient of the phantom was estimated as 0.61 mm^{-1} at the excitation wavelength.

Figure 2 shows characteristics of fluorescence modulation intensity in the scattering medium versus sound pressure in the ultrasound focus. Data were measured while varying the excitation voltage of the transducer at the position where the ultrasound focus corresponds to the fluorescent region site. Fluorescence modulation (signal) intensity is proportional to the square of the sound pressure, indicating a linear relationship between the sound power and the fluorescence signal intensity.

Figure 3(a) portrays a tomographic image of fluorescence observed with a phantom of light-scattering gel that contains a single fluorescent region in the center. A round shape of the fluorescence image is determined. Some correspondence is apparent: the area of higher signal intensity on the image indicates the embedded area of the localized fluorescent region in the phantom. Periodic changes of signal intensity that appeared along the Y axis are inferred to result from the presence of a standing wave formed in the phantom on the axis of the ultrasound beam. The profile of the signal intensity along the X axis on the image sectioned at the center of the phantom including the fluorescent region is shown in Fig. 3(b). The full width at halfmaximum of the profile is approximately 3 mm, corresponding to the diameter of the embedded fluorescent region. Considering the 3 mm beam diameter of a focused ultrasound field, the spatial resolution observed in the image is appropriate. A photograph of the phantom sectioned in the longitudinal plane is indicated in Fig. 3(c) with a dashed line of the scanned plane. Figure 4 depicts the observed result using a phantom that includes two fluorescent regions with an embedded 9 mm gap along the X axis. Both the image [Fig. 4(a)] and the X-axis profile [Fig. 4(b)] show the two well-separated fluorescence peaks, which

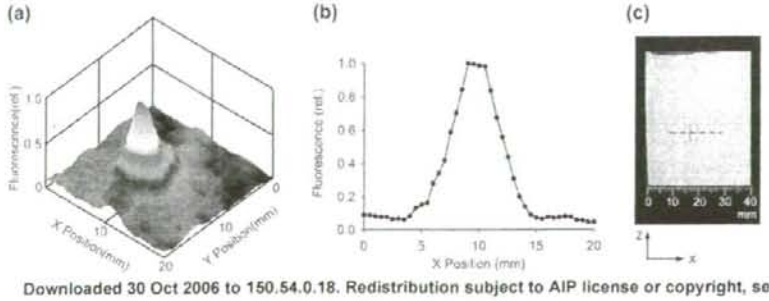

FIG. 3. (Color online) (a) Tomographic image of fluorescence observed with a phantom of light-scattering gel with a single fluorescent region in the phantom's center. (b) Profile of the signal intensity along with X axis on the image sectioned at the center of the phantom, which contains the embedded fluorescent region. (c) Photograph sectioned in the longitudinal plane of the phantom. An embedded fluorescent region is outlined. A dashed line shows the scanning plane of measurement.

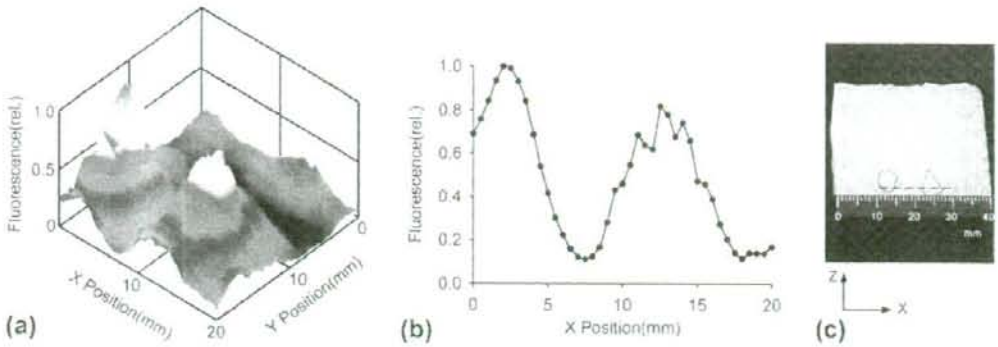

FIG. 4. (Color online) (a) Tomographic image of fluorescence observed with a phantom; the phantom was made of light-scattering gel with two fluorescent regions and a 9 mm gap. (b) Profile of the signal intensity along the X axis on the image sectioned at the center of the phantom, which contains the embedded fluorescent regions. (c) Photograph sectioned in the longitudinal plane of the phantom. Two embedded fluorescent regions are outlined. A dashed line shows the scanning plane of measurement.

correspond to the embedded positions of both regions, as shown in the photograph sectioned on the longitudinal plane of the phantom [Fig. 4(c)]. Taking into consideration the reduced scattering coefficient of the phantom, which is estimated as 0.61 mm^{-1} at the measured wavelength, this technique is potentially applicable for biological tissues. It can be used to obtain a tomographic image of fluorescence using near-infrared light. Although a quantitative comparison is necessary to apply this technique for absolute measurements of the distribution of fluorescence intensity, the results obtained here suggest that this simple method is potentially useful for imaging to resolve the position of a localized fluorescent region in a scattering medium. Considering this, further progress in the development of scanning techniques based on an array transducer can provide a method for measuring fluorescence buried in scattering media such as biological tissues. This technique is expected to facilitate the expansion of fluorescent probes' use for biological applications throughout the fields of life science and medicine.

This work was supported in part by grants from the Japanese Ministry of Education, Culture, Sports, Science, and Technology, from Innovation Plaza Miyagi, the Japan Science and Technology Agency, and from the Tohoku Institute of Technology.

[1]E. M. Sevick-Muraca, E. Kuwana, A. Godavarty, J. P. Houston, A. B. Thompson, and R. Roy, in *Biomedical Photonics Handbook*, edited by T. Vo-Dinh (CRC, Boca Raton, FL, 2003), 33, pp. 1.
[2]M. Toida, M. Kondo, T. Ichimura, and H. Inaba, Appl. Phys. B: Photophys. Laser Chem. **52**, 391 (1991).
[3]B. Devaraj, M. Takeda, M. Kobayashi, M. Usa, K. P. Chan, Y. Watanabe, T. Yuasa, T. Akatsuka, M. Yamada, and H. Inaba, Appl. Phys. Lett. **69**, 3671 (1996).
[4]M. Kempe, M. Larionov, D. Zaslavsky, and Z. Genack, J. Opt. Soc. Am. A **14**, 1151 (1997).
[5]G. D. Mahan, W. E. Engler, J. J. Tiemann, and E. Uzgiris, Proc. Natl. Acad. Sci. U.S.A. **95**, 14015 (1998).
[6]L. V. Wang, S. L. Jacques, and X. Zhao, Opt. Lett. **20**, 629 (1995).
[7]L. V. Wang, Phys. Rev. Lett. **87**, 043903 (2001).

Available online at www.sciencedirect.com
ScienceDirect
Biochemical and Biophysical Research Communications 351 (2006) 7–13
BBRC
www.elsevier.com/locate/ybbrc

Reduction in nonfluorescence state of quantum dots on an immunofluorescence staining

Songhua Li-Shishido [a], Tomonobu M. Watanabe [b], Hiroshi Tada [a], Hideo Higuchi [b,*], Noriaki Ohuchi [a]

[a] *Division of Surgical Oncology, Graduate School of Medicine, Tohoku University, Japan*
[b] *Biomedical Engineering Research Organization, Tohoku University, Japan*

Received 8 September 2006
Available online 9 October 2006

Abstract

Fluorescence quantum dots are widely used in immunofluorescence staining because of their intense and stable fluorescence. However, the nonfluorescence state of the quantum dots is their disadvantage. Here, the nonfluorescence state of the dots labeled to cells and tissues was suppressed. Cells and tissues where the receptor HER2 had been overexpressed were fixed and then labeled with anti-HER2 cross-linked with the dots. The intensity of the dots increased with the illumination time. The majority of the single dots were in the nonfluorescence state at beginning of the illumination period and the number of fluorescence dots observed increased with the illumination time. Living cells were also labeled with the anti-HER2-Qdots. Blinking and bleaching of the Qdots was effectively suppressed by adding β-mercaptoethanol and glutathione. Therefore, the movement of the Qdots bound to cell membrane could be observed for long periods of time.

Keywords: Quantum dots; Immunofluorescence; Fixed cell; Fixed tissue; Live cell; Imaging; Single particles; Single molecules; Nanotechnology

The fluorescence quantum dots (Qdots) are nanocrystals of semiconductor materials, for example, CdSe and CdTe [1–4]. The wavelength of the fluorescence of the Qdots changes with the diameter of the crystals. Small sized crystals (~2 nm in diameter of CdSe) emit blue fluorescence and larger crystals (~4 nm) emit red fluorescence [1]. The quantum yield of fluorescence emission is affected by the environmental conditions [5]. To get higher quantum yield of fluorescence, the Qdots were coated with the other semiconductor, for example, ZnS [5]. For use in biological experiments, the Qdots were coated further with a polymer which has reactive sites, amine or carboxyl groups, to conjugate with proteins, DNA and RNA [6]. After conjugation, the Qdots are imaged to determine the localization of target biological molecules and measure the number of target molecules [7–9].

The fluorescence intensity of the Qdots is considerably higher than that of organic dyes. They do not bleach for long period of time even in the absence of anti-fading reagents, which would destroy cell [8]. These advantages of the Qdots have been widely used in the biological and medical fields [3,10]. The disadvantage of the Qdots is that they bind reversibly to a nonfluorescence state which results in blinking and low fluorescence intensity [11–13]. To measure the number or intensity of the Qdots that have bound to cells, the intensity of each Qdot must be stable. To observe single Qdots labeled to proteins for long periods of time, the Qdots must emit fluorescence for long periods without blinking [13,14].

In this study, the nonfluorescence state (off-state) of the antibody–Qdot complex bound to the cells was reduced in order to improve the quantitative measurements and fluorescence period of the Qdots. The period at fluorescence

* Corresponding author. Fax: +81 22 795 5753.
E-mail address: higuchi@tubero.tohoku.ac.jp (H. Higuchi).

0006-291X/$ - see front matter © 2006 Elsevier Inc. All rights reserved.
doi:10.1016/j.bbrc.2006.09.159

state (on-state) of the Qdots bound to fixed and embedded cells increased with the time when that were illuminated by laser. The reducing agents, β-mercaptoethanol or glutathione, were inhibited the off-state.

Materials and methods

Qdot was conjugated to chimeric monoclonal antibody against HER2, trastuzumab (Herceptin, Chugai Pharmaceutical Ltd.) with Qdots 605, 655, and 705, where the number indicates the wavelength at maximum fluorescence. An antibody Conjugation Kit (Qdot corporation) was used [7,15] according to the manufacturer's instructions. The final concentration of trastuzumab–Qdots was determined by measuring the conjugate absorbance.

The human breast cancer cell line KPL-4, which overexpresses HER2 and is sensitive to trastuzumab [16,17], was kindly provided by Dr. J. Kurebayashi. KPL-4 cells were cultured in DMEM supplemented with 5% fetal bovine serum. MDA-MB-231 cells having a low expression of HER2 were maintained in L-15 medium, respectively, with 10% fetal bovine serum [16,18,19].

A suspension of KPL-4 cells was transplanted subcutaneously to the dorsal skin of female Balb/c nu/nu mice at ~5 weeks of age (Charles River). Several weeks after tumor inoculation, mice bearing a tumor with a volume of 100–200 mm^3 were selected. The mice were sacrificed with an overdose of CO_2. The tumors were removed and divided. All operations on animals were in accordance with the institutional animal use and care regulations.

For the immuno histochemical analysis, cells on a coverslip were fixed at 10% neutral-buffered formalin for 10 min [8]. Fixed cells were extensively washed three times with PBS solution. To minimize the nonspecific binding of trastuzumab-Q dot complexes to the cells, the cells were treated with the blocking solution containing NH_4Cl, glycine, FBS or BSA. The best treatment for blocking was incubating the cells in PBS solution containing 50 mM NH_4Cl for 10 min and then in 10% FBS for 30 min after a through washing with NH_4Cl.

The trastuzumab–Qdot complexes or polyclonal anti-HER2 cells from rabbit were reacted with the cells that had been blocked. The anti-HER2 cells were further reacted with anti-rabbit IgG conjugated with Qdots.

Tumors were fixed in 10% neutral-buffered formalin overnight [8] and then transferred into ethanol before processing and paraffin embedding. The tissue after removing paraffin was then treated with the PBS solution containing trastuzumab–Qdots. The fixed cells and tissue were embedded into Permafluor™ (Thermo Shandon).

Qdots were observed under microscopes (IX71 or BX51, Olympus) [20,21], equipped with green laser (532 nm), long pass filter (>580 nm). Fixed cells were observed at a power density of 11 (Fig. 1), or 31 W/mm^2 (Figs. 2–4). The x- and y-positions of the fluorescent spot were calculated by fitting the data to a 2D-Gaussian curve [21].

Results

The trastuzumab–Qdots bound well to KPL-4 cells but not to the MDA-MB-231 cells which expressed HER2 at low levels [19] (Fig. 1A and B). Most of the Qdots bound to the cell membrane (Fig. 1A). The intensity of the Qdots bound to the cells was measured in order to estimate the number of the bound Qdots. The Qdots without trastuzumab labeling did not bind to KPL-4 and MDA-MB-231 cells (Fig. 1C). The intensity of the Qdots bound to KPL-4 was approximately 10 times higher than those bound to MDA-MB-231 cells. This result was consistent with the expression of HER2 in these cells [19].

The trastuzumab–Qdots were bound to a tumor transplanted in a nude mouse. The trastuzumab–Qdots bound

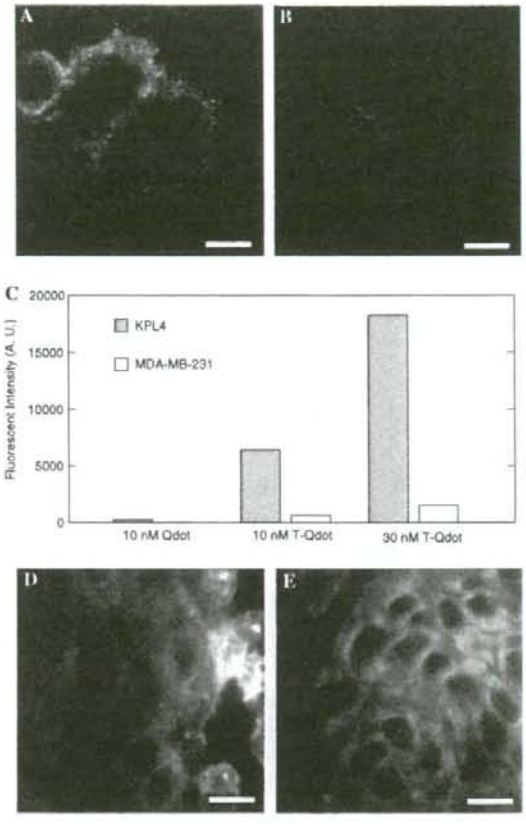

Fig. 1. Antibody–Quantum dot complex bound to cells and the tumor. Qdot705 (30 nM) labeled with trastuzumab bound to fixed KPL-4 cells (A) and MDA-MB-231 cells (B). (C) Fluorescence intensity of Qdots measured in several different cells. Open and closed bars indicate the intensity of KPL-4 and MDA-MB-231 cells, respectively. The two bars on the left-hand side show Qdots that have not bound trastuzumab after they had been mixed with the cells. Bars in the center and on the right show results in the presence of trastuzumab. (D) Sections of a tumor in a mouse, 5 μm thickness, were stained using Qdot-705 (10 nM) and labeled with trastuzumab. (E) The section was reacted with rabbit anti-HER2 and then with Qdot-705 (10 nM) labeled with anti-rabbit IgG. Scale bars = 10 μm (A, B, D, and E). Images were taken at an exposure time of 0.2 s at laser power of 11 W/mm^2.

mainly to the region near the KPL-4 cell membrane (Fig. 1D). The tumor also reacted with the polyclonal anti-HER2 cells from rabbits and then with anti-rabbit IgG labeled with the Qdots (Fig. 1E). The rabbit-IgG–Qdots bound to the cell membrane in similar areas where the trastuzumab–Qdots bound using direct staining methods (Fig. 1D and E). These results indicate that the fixed cells and tumor cells could be successively stained with antibodies labeled with the Qdots.

The change in fluorescence intensity of the antibody–Qdots was measured after illuminating the sections for long periods by a laser to test the stability of fluorescence emis-

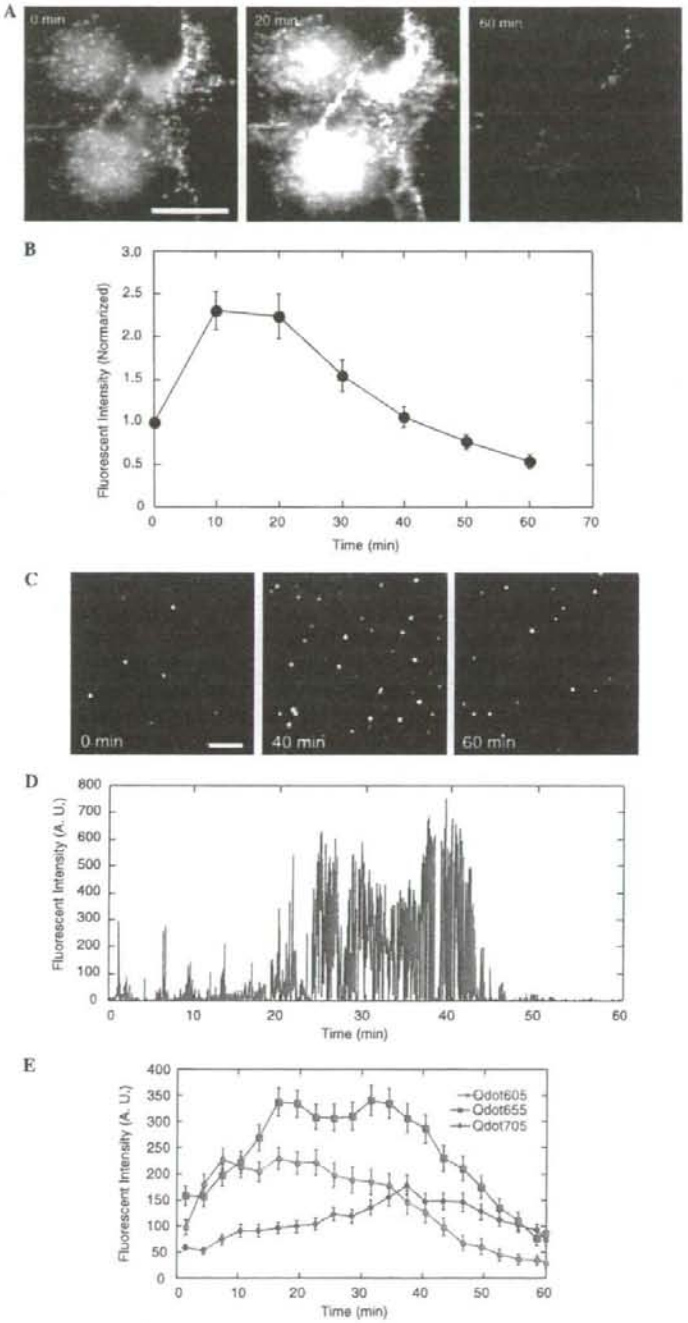

Fig. 2. Change in Qdot intensity when illuminated by a green laser. KPL-4 cells were labeled with trastuzumab–Qdot-705 (10 nM). Qdots were illuminated by the green laser at a laser power of 74 W/mm^2. (A) Images were taken at an exposure time of 0.05 s at illumination periods of 0, 20, and 60 min. Scale bar indicates 10 μm. (B) Intensity in several regions were measured. (C) Trastuzumab–Qdots-705 (0.1 nM) were spread on a coverslip. Images were taken at exposures time of 1 s at illumination periods of 0, 40, and 60 min using a laser power of 74 W/mm^2. Scale bar = 10 μm. (D) Intensity at several regions was measured at an exposure time of 1 s. (E) The average of hundreds of intensities from Qdots-605 (red symbols), 655 (blue), and 705 (green).

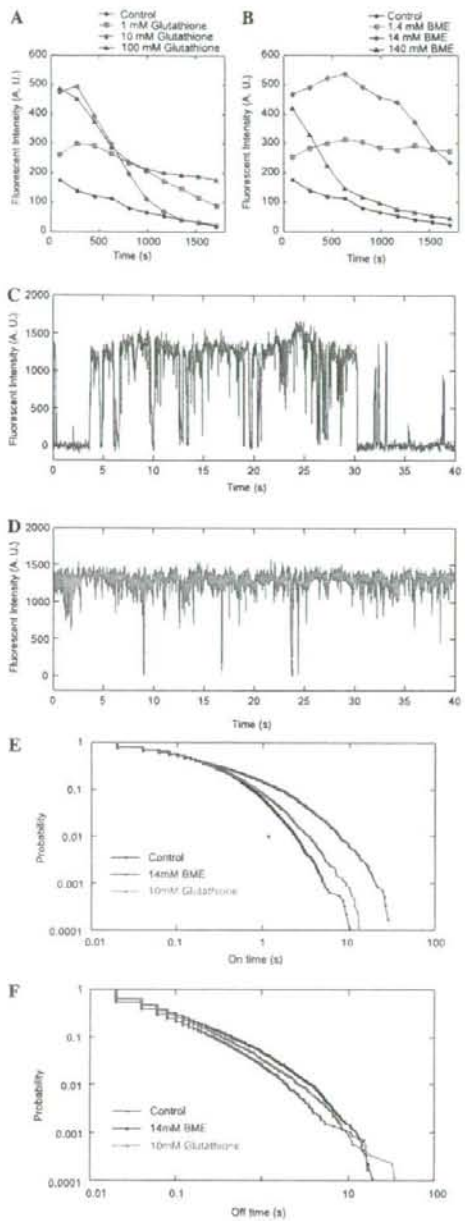

Fig. 3. The on- and off-dwell times in the presence of reducing agents. Qdot-655 (0.1 nM) in PBS solution containing BME (0, 1.4, 14, and 140 mM, (A)) and glutathione (0, 1, 10, and 100 mM, (B)) were spread on coverslips. Images were taken at exposure time of 1 s for 30 min at a laser power of 74 W/mm^2. (C,D) Images in the absence (C) and presence (D) of 14 mM BME were taken at beginning of the illumination period at exposure times of 20 ms and a laser power of 74 W/mm^2. (E,F) Fluorescence of the on- and off- dwell times was measured from the results shown in (C) and (D). The total dwell time was calculated from the probability.

sion. The power of green laser was increased by ~ 7 times to accelerate the intensity change. The intensity increased prominently 20 min into the illumination period (Fig. 2A). Sixty minutes into the illumination period, the intensity had returned to its original levels. The intensities at many regions in cells could be quantitatively analyzed relative to the initial intensity (Fig. 2B). In contrast, the fluorescence intensity of an organic fluorescence molecule, Cy3, conjugated to trastuzumab decreased exponentially with the illumination time (data not shown). The time constant was only 20 s.

To find the reason for this enhancement of intensity, the intensity of single Qdots embedded into Permafluor™ without being attached to cells was analyzed. Sequential images were taken every 1 s (Fig. 2C). The number of fluorescence Qdots appeared to increase, while the intensity of the bright Qdots changed little (Fig. 2C). Fig. 2D shows the intensity change in relation to the illumination time. The intensity of most Qdots increased firstly and decreased with time. During the periods where the Qdots exhibited their highest intensity, i.e., 20–43 min after the start of the illumination period (Fig. 2D), Qdots blinked from zero to maximum intensity. Assemble averages of the intensity of Qdot-705 showed that the intensity increased at the beginning and then gradually decreased to the end (Fig. 2E). The other Qdots, 605 and 705, showed similar intensity profiles to the Qdot-655 but had different time constants.

Fluorescence imaging is also used for position measurements of proteins [21,22]. To observe the position of Qdots bound to living cells, we determined the most suitable conditions that allowed Qdots to bind for long periods of time with high spatial and temporal precision [21]. The reducing reagent, DTT and β-mercaptoethanol (BME), are known to suppress the blinking but its effects on the bleaching time have not been determined [13]. We investigated the effect of BME and glutathione on both the bleaching and blinking. The intensity increased several fold in the presence of the reducing agents comparing to that in the absence (Fig. 3A and B). The intensity decreased with the time illuminated by the laser. The intensity in the presence of 1 and 100 mM glutathione, 1.4 and 14 mM BME suppressed the reduction of intensity for long time (30 min). In the presence of 10 mM glutathione and 140 mM BME, the intensity was reduced only at the beginning (<20 min) and not thereafter.

To analyze the blinking of the fluorescence intensity, the temporal resolution of the imaging was improved to be 20 ms (Fig. 3C and D). In the absence of the reducing agent, the Qdots blinked frequently and showed long dwell times in the off-state. In the presence of BME, the Qdots emitted the fluorescence continuously for long periods of time without spending long periods in the off-state. To evaluate the suppression of blinking, the dwell times of on and off-states were analyzed [13]. The probability of Qdots being in the state of long on-dwell time in the presence of BME is much higher than that in the absence of BME. For example, the probabilities of Qdots having on-

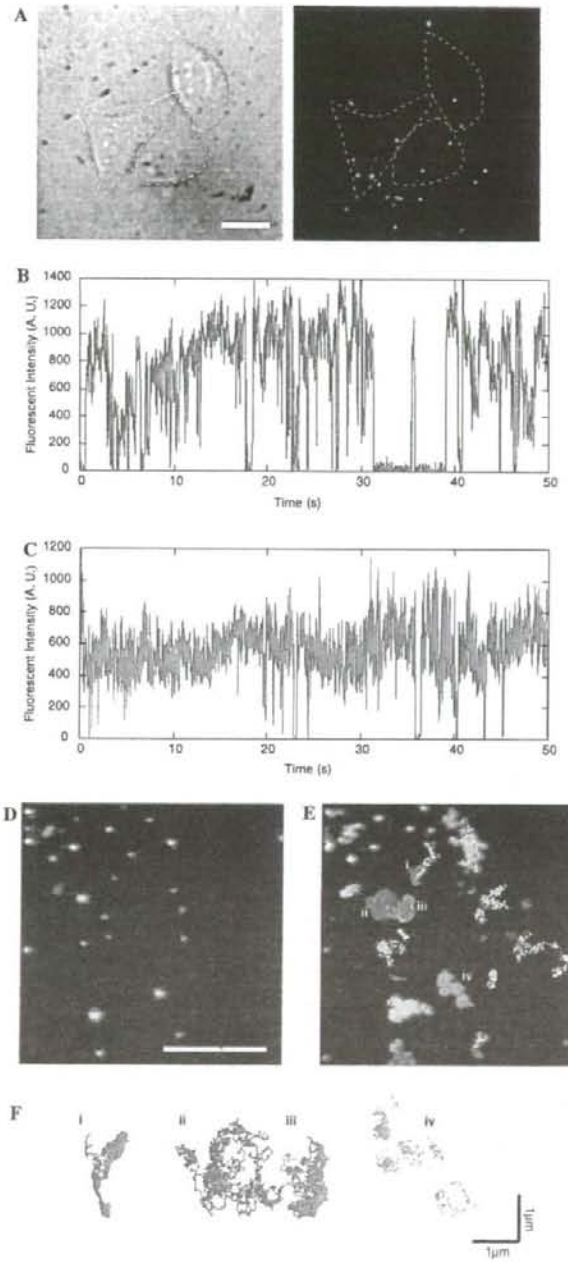

Fig. 4. Blinking of Qdots bound to living cells. Qdots-655 (0.5 nM) labeled with trastuzumab were bound to living KPL-4 cells. (A) There are a bright field (left) and fluorescence (right) images of the cells. Dotted lines indicate the edge of the cells. Scale bar = 10 μm. The blinking of Qdots in the absence (B) and presence (C) of 14 mM BME is shown at an exposure time of 20 ms. (D) Fluorescence images of Qdots were taken under a total internal reflection microscope at an exposure time of 20 ms and laser power of ~70 W/mm^2. Scale bar = 5 μm. (E) The Qdots bound to cells were taken at a higher magnification. To trace the movement of Qdtos, 2500 images were collected over a 50 s period and then superimposed. Colored lines indicate the traces of single Qdots. (F) Traces indicate movements of Qdots that occurred on the cell membrane for a 50 s period.

dwell times of 5 s are approximately 2.3% in the presence of BME which are considerably higher than 0.10% in the absence of BME. The off-dwell time is also higher in the absence of BME. Long on-dwell times and short off-dwell times observed in the presence of BME indicate that the Qdots stay in the on-state for most of the time.

The imaging of proteins in living cells is an important application of Qdots. The trastuzumab–Qdot complexes were mixed with living cells to detect the movement of membrane receptor, HER2, in the presence of BME. The movement of the Qdots was measured within the first 30 min when the activity of the cells was not altered.

The trastuzumab–Qdot complexes bound to the membrane of the cells (Fig. 4A). Qdots in the absence of BME often exhibited blinking (Fig. 4B). Most on-dwell times were less than 1 s. The long off-dwell times were common. In the presence of 14 mM BME, the on-dwell times became longer than 1 s for many of the Qdots (Fig. 4C). The off-dwell time was very short <0.2 s (Fig. 4C).

The position of the Qdots bound to cell membrane was measured by fitting the data of the fluorescence of the spots to two-dimensional Gaussian with one nanometer precision [21,23]. Fig. 4D shows the initial image of the Qdots bound to the cell membrane. All images have been superimposed as shown in Fig. 4E. The center of the fluorescence spots was measured continuously for 50 s without losing the data by off-dwell (colored traces in Fig. 4E). Traces on an expanded time scale show the detailed movement of the Qdots (Fig. 4F). Most of the Qdots moved a distance of 3 μm in 50 s which is considerably shorter than that of free diffusion of trastuzumab–Qdots (~30 μm assuming the diameter of 30 nm). The some of movements of the Qdots were random (Fig. 4F(i and ii)). Some of the Qdots moved within a narrow area (iii). Other Qdots moved within small area and then hoped to the next area (iv).

Discussion

The intensity of the Qdots bound to KPL-4 cells was approximately 10 times higher than that to MDA-MB-231 cells. This result is consistent with the expression HER2 in these cells [16,18,19]. The advantage of Qdot immunofluorescence staining is that quantitative analysis of bound Qdots to cells is possible. Another advantage is the higher sensitivity as even single Qdots can be imaged (Figs. 2C and 4D) [13,14,21]. The trastuzumab–Qdots also bound selectively to a tumor formed by KPL-4 cells transplanted in a nude mouse, suggesting this technique has applications for medical immunohistochemistry [3,24,25].

Organic fluorescent dyes for immunofluorescence staining are not suitable for quantitative analysis because of their low intensity and rapid bleaching within 20 s of illumination [8]. The trastuzumab–Qdots remained stable for periods up to 1 h (Fig. 2) [8,13,26,27]. The intensity of the Qdots did not change much in the first ~10 min after laser illumination (Fig. 2E). The intensity then gradually increased to 2–3 times of from the initial intensity and then decreased [26]. These changes in intensity were also obtained for Qdots labeled cells stored in the Permafluor for 3 months at room temperature (data not shown). These results indicate that Qdots are very useful for quantitative analysis of immunofluorescence staining even when they have been stored for long periods.

Measurements of the intensity of single Qdots indicated that the number of Qdots at the fluorescence on-state increases with time (Fig. 2). The single Qdots were bleached by long-term continuous illumination with a laser. These changes in intensity of single Qdots explain the change in intensity of multiplied Qdots bound to cells (Fig. 2). Single Qdots analysis is a powerful method to determine the fundamental properties of Qdots [14,21].

The reducing agents, BME and DTT, suppressed the blinking of intensity of Qdots [13]. The intensity of Qdots in the presence of BME and glutathione was measured. BME (1.4 mM or higher) and glutathione (1 mM or higher) considerably enhanced the on-dwell time and shortened the off-dwell time marginally. The on-dwell time was enhanced in the presence of 14 mM BME but not in the presence of 140 mM BME. The enhancement of on-dwell time by the reducing agents was consistent with the previous results [13].

The longer on-dwell times and shorter off-dwell times increased the possibility that Qdots would stay in the on-state (Fig. 3C–F). Therefore, the total intensity of Qdots increased considerably at the beginning of the illumination period (Fig. 3A and B). Illumination for long periods using a laser resulted in the Qdots bleaching and the total intensity gradually decreasing. The decay time of the intensity by photobleaching was slowest in the presence of 14 mM BME. At higher concentrations of BME (140 and 280 mM), the intensity decay time was shorter. The optimum conditions for suppressing the bleaching and blinking were 14 mM BME.

Qdots bind to proteins in both *in vitro* motility assays and in cells [14,21]. The higher intensity of the fluorescence has made it possible to precisely detect the position of Qdot within a few nanometers and milliseconds. Because many of Qdots did not exhibit the blinking for >10 s, the Qdot position was measured for long time without missing the data by blinking (Fig. 4D–F). The movements of Qdots are much slower than that at free diffusion. Some of Qdots showed the hopping movement from the one area to the other, which is consistent with previous reports [28].

Stable and intense fluorescence of Qdots are advantageous for fluorescence imaging. However, blinking and non-specific binding of Qdots must be acknowledged as potential problems. Here non-specific binding was avoided by the improvement of blocking method. The off-state of Qdots bound to fixed and embedded cells was suppressed by the illumination of laser. The blinking of Qdots bound to living cells were suppressed effectively in the presence of 14 mM BME. These improvements open-up the new applications of Qdots such as medical immunostaining and nanometer measurement of position.

Acknowledgments

We thank Ms. Sachiko Higuchi and Dr. J.M. West for helping. This work was supported by Grants-in-Aid for Research Project, Promotion of Advanced Medical Technology (N.O.), Scientific Research in Priority Areas from the Japan MEXT (H.H.), and Special Coordination Funds for Promoting Science and Technology of Japan (H.H., T.M., and N.O.).

References

[1] M. Bruchez Jr., M. Moronne, P. Gin, S. Weiss, A.P. Alivisatos, Semiconductor nanocrystals as fluorescent biological labels, Science 281 (1998) 2013–2016.
[2] W.C. Chan, S. Nie, Quantum dot bioconjugates for ultrasensitive nonisotopic detection, Science 281 (1998) 2016–2018.
[3] X. Gao, Y. Cui, R.M. Levenson, L.W. Chung, S. Nie, In vivo cancer targeting and imaging with semiconductor quantum dots, Nat. Biotechnol. 22 (2004) 969–976.
[4] X. Michalet, F.F. Pinaud, L.A. Bentolila, J.M. Tsay, S. Doose, J.J. Li, G. Sundaresan, A.M. Wu, S.S. Gambhir, S. Weiss, Quantum dots for live cells, in vivo imaging, and diagnostics, Science 307 (2005) 538–544.
[5] X. Peng, M.C. Schlamp, A.V. Kadavanich, A.P. Alivisatos, Epitaxial growth of highly luminescent CdSe/CdS core/shell nanocrystals with photostability and electronic accessibility, J. Am. Chem. Soc. 119 (1997) 7019–7029.
[6] W.C. Chan, D.J. Maxwell, X. Gao, R.E. Bailey, M. Han, S. Nie, Luminescent quantum dots for multiplexed biological detection and imaging, Curr. Opin. Biotechnol. 13 (2002) 40–46.
[7] I.L. Medintz, H.T. Uyeda, E.R. Goldman, H. Mattoussi, Quantum dot bioconjugates for imaging, labeling and sensing, Nat. Mat. 4 (2005) 435–446.
[8] X. Wu, H. Liu, J. Liu, K.N. Haley, J.A. Treadway, J.P. Larson, N. Ge, F. Peale, M.P. Bruchez, Immunofluorescent labeling of cancer marker Her2 and other cellular targets with semiconductor quantum dots, Nat. Biotechnol. 21 (2003) 41–46.
[9] D.S. Lidke, P. Nagy, R. Heintzmann, D.J. Arndt-Jovin, J.N. Post, H.E. Grecco, E.A. Jares-Erijman, T.M. Jovin, Quantum dot ligands provide new insights into erbB/HER receptor-mediated signal transduction, Nat. Biotechnol. 22 (2004) 198–203.
[10] B.N. Giepmans, T.J. Deerinck, B.L. Smarr, Y.Z. Jones, M.H. Ellisman, Correlated light and electron microscopic imaging of multiple endogenous proteins using Quantum dots, Nat. Methods 2 (2005) 743–749.
[11] M. Nirmal, B.O. Dabbousi, M.G. Bawendi, J.J. Macklin, J.K. Trautman, T.D. Harris, L.E. Brus, Fluorescence intermittency in single cadmium selenide nanocrystals, Nature 383 (1996) 802–804.
[12] G. Schlegel, J. Bohnenberger, I. Potapova, A. Mews, Fluorescence decay time of single semiconductor nanocrystals, Phys. Rev. Lett. 88 (2002) 137401.
[13] S. Hohng, T. Ha, Near-complete suppression of quantum dot blinking in ambient conditions, J. Am. Chem. Soc. 126 (2004) 1324–1325.
[14] D.M. Warshaw, G.G. Kennedy, S.S. Work, E.B. Krementsova, S. Beck, K.M. Trybus, Differential labeling of myosin V heads with quantum dots allows direct visualization of hand-over-hand processivity, Biophys. J. 88 (2005) L30–L32.
[15] X. Gao, L. Yang, J.A. Petros, F.F. Marshall, J.W. Simons, S. Nie, In vivo molecular and cellular imaging with quantum dots, Curr. Opin. Biotechnol. 16 (2005) 63–72.
[16] J. Kurebayashi, T. Otsuki, C.K. Tang, M. Kurosumi, S. Yamamoto, K. Tanaka, M. Mochizuki, H. Nakamura, H. Sonoo, Isolation and characterization of a new human breast cancer cell line, KPL-4, expressing the Erb B family receptors and interleukin-6, Br. J. Cancer 79 (1999) 707–717.
[17] J. Kurebayashi, Regulation of interleukin-6 secretion from breast cancer cells and its clinical implications, Breast Cancer 7 (2000) 124–129.
[18] H. Kunisue, J. Kurebayashi, T. Otsuki, C.K. Tang, M. Kurosumi, S. Yamamoto, K. Tanaka, H. Doihara, N. Shimizu, H. Sonoo, Anti-HER2 antibody enhances the growth inhibitory effect of anti-oestrogen on breast cancer cells expressing both oestrogen receptors and HER2, Br. J. Cancer 82 (2000) 46–51.
[19] K. Fujimoto-Ouchi, F. Sekiguchi, Y. Tanaka, Antitumor activity of combinations of anti-HER-2 antibody trastuzumab and oral fluoropyrimidines capecitabine/5′-dFUrd in human breast cancer models, Cancer Chemother. Pharmacol. 49 (2002) 211–216.
[20] V.T. Nguyen, Y. Kamio, H. Higuchi, Single-molecule imaging of cooperative assembly of gamma-hemolysin on erythrocyte membranes, EMBO J. 22 (2003) 4968–4979.
[21] S. Toba, T.M. Watanabe, L. Yamaguchi-Okimoto, Y.Y. Toyoshima, H. Higuchi, Overlapping hand-over-hand mechanism of single molecular motility of cytoplasmic dynein, Proc. Natl. Acad. Sci. USA 103 (2006) 5741–5745.
[22] M. Ueda, Y. Sako, T. Tanaka, P. Devreotes, T. Yanagida, Single-molecule analysis of chemotactic signaling in dictyostelium cells, Science 294 (2001) 864–867.
[23] A. Yildiz, J.N. Forkey, S.A. McKinney, T. Ha, Y.E. Goldman, P.R. Selvin, Myosin V walks hand-over-hand: single fluorophore imaging with 1.5-nm localization, Science 300 (2003) 2061–2065.
[24] S. Kim, Y.T. Lim, E.G. Soltesz, A.M. De Grand, J. Lee, A. Nakayama, J.A. Parker, T. Mihaljevic, R.G. Laurence, D.M. Dor, L.H. Cohn, M.G. Bawendi, J.V. Frangioni, Near-infrared fluorescent type II quantum dots for sentinel lymph node mapping, Nat. Biotechnol. 22 (2004) 93–97.
[25] N.Y. Morgan, S. English, W. Chen, V. Chernomordik, A. Russo, P.D. Smith, A. Gandjbakhche, Real time in vivo non-invasive optical imaging using near-infrared fluorescent quantum dots, Acad. Radiol. 12 (2005) 313–323.
[26] Z. Zhelev, R. Jose, T. Nagase, H. Ohba, R. Bakalova, M. Ishikawa, Y. Baba, Enhancement of the photoluminescence of CdSe quantum dots during long-term UV-irradiation: privilege or fault in life science research? J. Photochem. Photobiol. B: Biol. 75 (2004) 99–105.
[27] K. Hanaki, A. Momo, T. Oku, A. Komoto, S. Maenosono, Y. Yamaguchi, K. Yamamoto, Semiconductor quantum dot/albumin complex is a long-life and highly photostable endosome marker, Biochem. Biophys. Res. Commun. 302 (2003) 496–501.
[28] K. Suzuki, K. Ritchi, E. Kajikawa, T. Fujiwara, A. Kusumi, Rapid hop diffusion of a G-protein coupled receptor in the plasma membrane as revealed by single-molecule techniques, Biophys. J. 88 (2005) 3659–3680.

ELSEVIER

Journal of Alloys and Compounds 434–435 (2007) 718–720

Journal of ALLOYS AND COMPOUNDS

www.elsevier.com/locate/jallcom

Photocurrent of nanoassembled Si film in contact with electrolyte

S. Mamykin [a,*], A. Kasuya [a], A. Dmytruk [a], N. Ohuchi [b]

[a] *Center for Interdisciplinary Research, Tohoku University, Sendai 980-8578, Japan*
[b] *Graduate School of Medicine, Tohoku University, Sendai 980-8579, Japan*

Available online 12 October 2006

Abstract

Nanoassembled Si thin films on conducting glass have been prepared. Films are photoactive and demonstrate "n-type" behavior in contact with electrolyte. Good correlation has been found between band gap obtained from luminescence and photocurrent. Up to such a small particle sizes the Si is still indirect optical material. Si nanoparticles demonstrate significantly reduced electron affinity 2.4 eV with much higher position of the bottom of conducting band compared to bulk Si while position of valence band did not change.

Keywords: Thin films; Electrode materials; Electronic band structure; Luminescence; Photocurrent

1. Introduction

Porous Si is a material of interest because of fundamental physical properties of quantum sized objects and possible promising applications in Si-based industry. Nanosized crystallites (<5 nm) have electrical and optical properties which are different from the bulk Si. Large specific surface area, increased band gap, luminescence in the visible region, changed electronic structure are basic properties used to design different devices such as solar cells with antireflecting coating [1], gas sensors, cold cathodes, flat panels, super capacitors, etc. [2,3]. It has also been proposed to use porous Si to improve hydrogen generation by p-Si in photoelectrolyses [4].

The usual way is to study porous Si on the Si wafer used for preparation. Unfortunately, in many cases, it is difficult to separate the properties of highly resistive, some times very thin layer of nanosized Si from the bulk material. The purpose of this report is to show a simple way to examine optical and photoelectrochemical properties of nanosized Si without influence of bulk Si. Prepared porous Si was separated from Si wafer and deposited as film on different substrate (conducting glass).

2. Experimental

Si nanoparticles were made by anodic etching of 0.12 Ω cm (1 0 0) p-type Si wafer with following dispersion of particles in toluen:ethanol (2:1) mixture by ultrasonic bath. The piece of Si wafer of rectangular form with 2 cm width was immersed into electrolyte on depth of 5 mm. Anodic current was about 40 mA/cm^2 and processing time was 15 min. HF (46%):H_2O_2 (30%):methanol (97%) 3:3:1 mixture was used as electrolyte. After anodization and before ultrasonic bath, the porous Si was carefully rinsed by methanol. Films were prepared by electrophoretic deposition [6] of Si nanoparticles on conducting glass from suspension. Deposited films were calcinated at 150 °C in N_2 atmosphere. As prepared films have yellow color and demonstrate interference maxima and minima during transmittance measurements suggesting films uniformity. The thickness measured by SEM was about 1 μm (Fig. 1). Spectra of luminescence have been measured by Jusco FP-750 spectrofluorometer. Photoelectrochemical measurements were carried out in 0.1 M H_2SO_4 electrolyte. CHI440 potentiostat and three-electrode cell was used to record photocurrent. All potentials are versus $Ag/AgCl_2$ reference electrode. Thousand Watts Xenon lamp with monochromator was used as source of white and monochromatic light. Actual white light intensity was 60 mW/cm^2.

3. Results and discussion

Freshly prepared (dispersed in toluene:ethanol) Si nanoparticles show luminescence with peak at 2.28 eV (545 nm, Fig. 2). From luminescence maximum, the particle size can be estimated to be around ~2 nm [5]. Excitation spectrum (dashed curve in Fig. 2.) is proportional to absorption and can be used to estimate optical band gap which is about 2.5 eV.

Photoelectrochemical properties of films have been studied in 0.1 M H_2SO_4 electrolyte using three-electrode cell. Working electrode demonstrates different potentials in darkness and under white light (Fig. 3) at the open circuit conditions. This photovoltage is about 0.5 V and shows "n-type" behavior. It suggests more than 0.5 V band bending at the equilibrium. The polarity of the voltage says that photogenerated electrons go to substrate

* Corresponding author. Tel.: +81 22 795 57 58; fax: +81 22 795 57 50.
E-mail address: mamykin@cir.tohoku.ac.jp (S. Mamykin).

0925-8388/$ – see front matter © 2006 Elsevier B.V. All rights reserved.
doi:10.1016/j.jallcom.2006.08.121

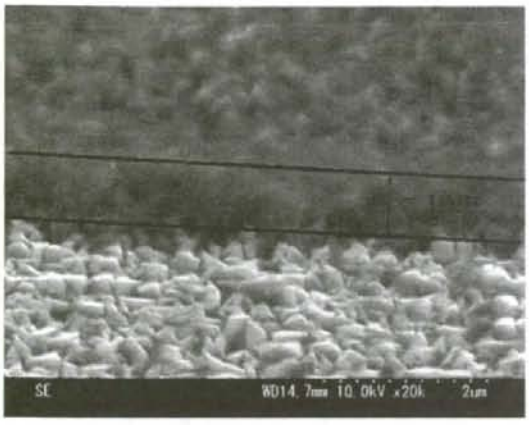

Fig. 1. SEM image of scratched and tilted sample. Si film thickness is about 1 μm.

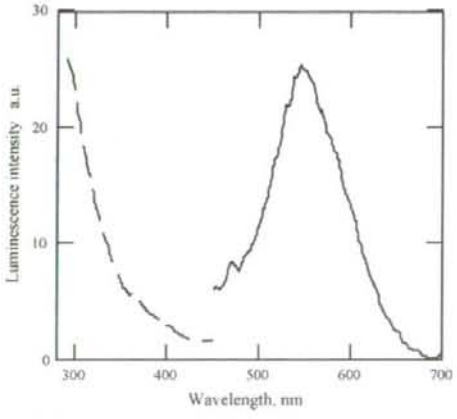

Fig. 2. Emission spectra (solid curve) and excitation (dashed curve) of luminescence of freshly prepared Si nanoparticles in toluene/ethanol mixture.

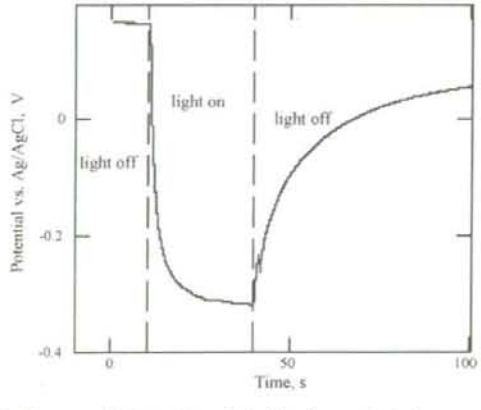

Fig. 3. Photopotential of sample vs. $Ag/AgCl_2$ reference electrode measured in 0.1 M H_2SO_4 electrolyte.

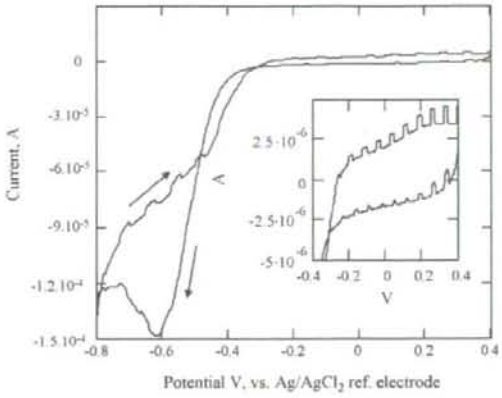

Fig. 4. Cyclic voltammetry under chopped white light of 60 mW/cm² intensity. The inset shows enlarged region of small current.

and holes go to contact with electrolyte. So, originally p-type Si was converted to n-type Si nanoparticles. This is in the agreement with high internal resistance of porous Si [2].

Cyclic voltammetry (Fig. 4) measured under chopped light allows to measure photo and dark current simultaneously. Significant dark current at negative potentials was present caused by reaction between substrate (fluorine doped SnO_2) and electrolyte. After dark current subtraction, the photocurrent (Fig. 5) shows three significant regions. The first is from 0.4 to −0.2 V. It increases from negative to positive potential with increasing of electric field in nanoparticles helping to separate photogenerated charge. This photocurrent is relatively small due to lack of hole scavenging at contact with electrolyte. Probably, the main holes consumer is oxidation reaction of Si. Second region is from −0.6 to −0.2 V. The photocurrent significantly increases due to increasing of reaction probability between generated holes and hydrogen. Third region is from −0.6 to negative side of potential. The photocurrent decreases with decreasing of electric field inside of Si particle at more negative potentials and riches zero at

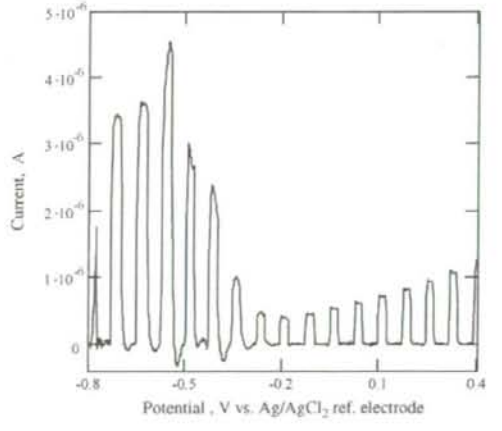

Fig. 5. Photocurrent of Si nanoparticles vs. applied potential.

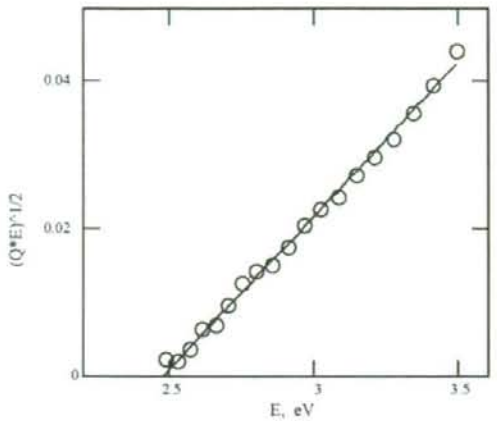

Fig. 6. Spectral dependence of quantum yield (Q) vs. photon energy. Special scale was applied to show indirect optical transitions. Measured optical band gap is 2.5 eV.

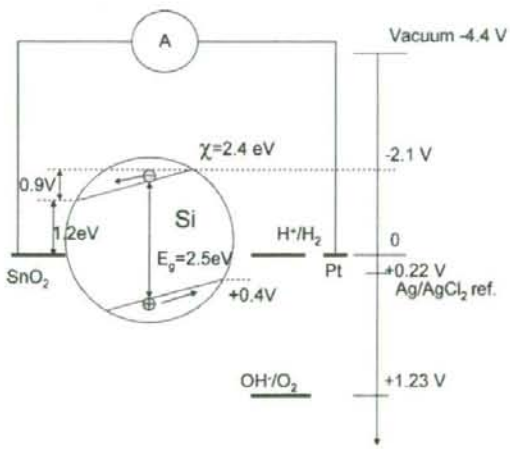

Fig. 7. Bands positions for Si nanoparticles in contact with electrolyte.

flat bands. Estimated flat band potential is about −0.9 V versus $Ag/AgCl_2$ reference electrode.

Spectral dependence of photocurrent was recorded at fixed applied bias (+0.2 V) where short circuit condition is performed. Behavior of the photocurrent quantum yield (Q) versus photon energy (Fig. 6) demonstrates indirect band gap 2.48 eV. This is much higher than band gap of bulk Si (1.12 eV) due to quantum size effect.

On the basis of obtained band gap (2.48 eV) and flat band potential (−0.9 V) it is possible now to estimate the electron affinity χ and band positions of nanosized Si (Fig. 7). Taking into account the low concentrations of free carriers due to trap by surface states [2], the Fermi level is fixed at the middle of band gap. Summarizing, the flat band potential (−0.9 V) and distance between Fermi level and bottom of conduction band (−1.25 V), the position of conduction band against $Ag/AgCl_2$ is found to be −2.15 V. Valence band position can be found by subtracting the value of band gap (2.5 eV) and it is +0.35 V. Electron affinity as distance between bottom of conduction band and vacuum level can be found using potential of $Ag/AgCl_2$ in vacuum scale (+4.6 eV) and it is ~2.4 eV. This is significantly lower then for bulk Si (3.8 eV). It is interesting to mention that valence band position of bulk Si (+0.4 versus $Ag/AgCl_2$) is almost the same as in the case of nanosized Si.

4. Conclusions

Nanoassembled Si films on conducting glass are photoactive and demonstrate "n-type" behavior. Good correlation has been found between band gap obtained from luminescence and photocurrent. Up to such a small particle sizes, the Si is still an indirect optical material. Si nanoparticles demonstrate significantly reduced electron affinity 2.4 eV with much higher position of the bottom of conducting band compared to bulk Si while position of valence band did not change.

References

[1] P. Menna, G. Di Francia, V. La Ferrara, Solar Energy Mater. Solar Cells 37 (1995) 13.
[2] V. Lehmann, Electrochemistry of Silicon, Wiley-VCH/Verlag GmbH, Weinheim, 2002.
[3] H. Foll, M. Christophersen, J. Carstensen, G. Hasse, Mater. Sci. Eng. R 39 (2002) 93.
[4] N.R. Mathews, P.J. Sebastian, X. Mathew, V. Agarwal, Int. J. Hydrogen Energy 28 (2003) 629.
[5] M.V. Wolkin, J. Jorne, P.M. Fauchet, G. Alan, C. Delerue, Phys. Rev. Lett. 82 (1999) 197.
[6] H. Li, C. Xue, H. Zhang, C. Guo, C. Li, L. Chen, Z. Diao, Int. J. Mod. Phys. B 16 (2002) 4306.

Journal of Nanoparticle Research (2007) 9:1067–1071
DOI 10.1007/s11051-006-9186-2

Research Paper

Organic-ligand-assisted supercritical hydrothermal synthesis of titanium oxide nanocrystals leading to perfectly dispersed titanium oxide nanoparticle in organic phase

Tahereh Mousavand, Jing Zhang, Satoshi Ohara, Mitsuo Umetsu, Takashi Naka and Tadafumi Adschiri*
*Institute of Multidisciplinary Research for Advanced Materials, Tohoku University, 2-1-1 Katahira, Aoba-ku, Sendai, 980-8577, Japan; *Author for correspondence (Tel.: +81-22-2175629; Fax: +81-22-2175631; E-mail: ajiri@tagen.tohoku.ac.jp)*

Received 3 March 2006; accepted in revised form 21 October 2006

Key words: dispersion, metal oxide, mixing, nanoparticle, supercritical hydrothermal synthesis

Abstract

Titanium oxide (TiO_2) nanocyrstals which are perfectly dispersed in organic solvents are synthesized by organic-ligand-assisted supercritical hydrothermal synthesis. The addition of hexaldehyde to the supercritical hydrothermal synthesis of TiO_2 leads to the *in-situ* surface modification, which enables the synthsized TiO_2 nanocrystals to be perfectly dispersed in iso-octane because of its hydrophobic nature. Further, the one-pot synthesis of hybrid materials results in the significant reduction of the particles size, probably due to the capping effect of hexaldehyde to suppress the particles growth.

Introduction

Metal oxide nanoparticles have been extensively investigated due to their present successful application and the foresight of their use in various fields of electronics, catalysis, pharmaceutics, energy storage and medical applications. Physical and chemical properties of the nanoparticles are varied by changing the size and morphology of the nanoparticles. The organization of these nanoparticles into functional systems has been expected as the expression of unique electric, photonic, and magnetic functions. For organizing the inorganic nanostructures, hybridization with organic materials is one of the attracting methods because various self-fabrications controlled by molecular structure can be utilized (Li et al., 2003). The surface on metal oxide particle is generally so hydrophilic by the presence of hydroxyl groups that the metal oxide particles are not well dispersed in an organic phase. In addition, the extremely high surface energy of nanoparticles leads to the aggregation of the nanoparticles (Singhal et al., 1999; Sanchez et al., 2001).

In order to attain good dispersion of metal oxide nanoparticles in organic phase, the utilization of a dispersing agent or the formation of hydrophobic surface layer around the nanoparticles is necessary (Bonnemann et al., 1996; Horn & Rieger et al., 2001); however, the present methods are not always applied for metal oxide particles. Recently, we have succeeded in the synthesis of various organic–inorganic hybrid materials in supercritical water with alcohol, aldehyde, carboxylic acids, or amine as the organic ligand, and reported that the organic molecule with an aldehyde group can change the surface properties of titanium oxide (TiO_2) materials (Mousavand et al., 2006a, b).

Here, we propose an one-pot synthesis of a surface-modified TiO_2 nanoparticle in supercritical fluid for spontaneous dispersion of the particle in non-polar organic phase.

Experimental

A 0.01 M TiO_2 colloid solution (ISHIHARA SANGYO KAISHA, Ltd. (Japan), the colloid size: 30 nm) and a 0.1 ml of hexaldehyde ($CH_3(CH_2)_4CHO$) was loaded into a pressure-resistant vessel (SUS316) with 5 ml of inner volume. The reactor was heated and shaken for 10 min in an electric furnace which controlled external surface temperature of the reactors at 200°C and 400°C. During the reactions, the pressures inside the reactor were 20 MPa and 40 MPa at 200 and 400°C, respectively. A 0.01 M $Ti(SO_4)_2$ solution was also used as a starting material to conduct the experiments with the same procedure as for the TiO_2 colloid solution. The ratio of organic modifier to aqueous solution was 38:1. The products were exported from the reactor into a beaker and were purified by repeating with decantation and centrifugation in ethanol several times. The purified products were transported into a two-phase mixture of water and chloroform, or water and iso-octane, in order to observe the dispersibility of the products in the organic phase.

The products were analyzed by X-ray diffractometry (XRD), infrared spectroscopy, thermogravimetry analysis (TGA), and electron microscopy. The XRD data were measured on a Dmax γ_B X-ray diffractometer (Rigaku) with CuKα radiation. For analyzing the organic molecules contained in the products, attenuated total reflectance (ATR) Fourier transform infrared (FT-IR) spectra were measured with a FT-IR-680 plus spectrometer (Jasco, Tokyo, Japan) at a resolution of 4 cm^{-1}. TGA was performed by a Thermo Plus (Rigaku) under a constant flow of argon gas at the heating rate of 10°C min^{-1}. The size and morphology of the prodcuts were observed with a transmission electron microscopy (TEM, JEM-1200 EX II (JEOL, Ltd.)).

Results and discussion

Figure 1 shows the products obtained from the TiO_2 colloid, in the separated liquids of water and chloroform (a, b), and water and isooctane (c, d). The TiO_2 particles obtained at 200°C without hexaldehyde were dispersed in water (shown in Figure 1a), similarly to the untreated TiO_2 particles, while those heated with hexaldehyde were dispersed in a chloroform phase (shown in Figure 1b). The heat treatment with the organic molecules changes the surface property of the TiO_2 particles, and the property change implies the immobilization of the organic molecules on the TiO_2 particles. However, the surface-modified TiO_2 particles were not dispersed to the organic phase in the mixture of water and iso-octane, as well as the unmodified TiO_2 particles (shown in Figure 1c, d). The TiO_2 particles treated at 400°C with hexaldehyde showed the same result (data not shown). The amount of immobilized organic molecules on the TiO_2 particles might not be

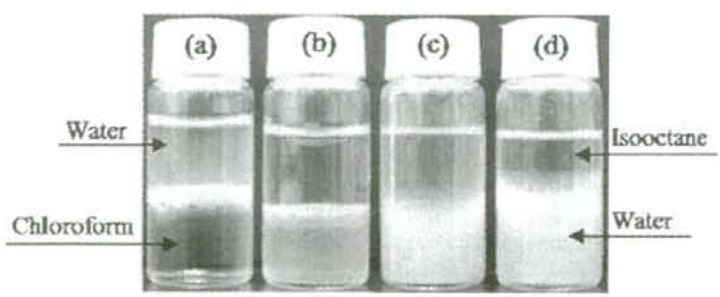

Figure 1. Dispersibility of colloidal TiO_2: (a, c) in a mixture of water and chloroform, (b, d) in a mixture of water and iso-octane. (a, c) colloidal TiO_2 treated at 200°C; (b, d) colloidal TiO_2 heated at 200°C in a mixture of water and iso-octane with hexaldehyde.

sufficient for goods dispersion in an non-polar organic solvent, nor the starting materials, TiO_2 colloid, might not have enough binding sites for the organic ligands to react.

Thus, we attempted the *in-situ* surface modification during supercritical hydrothermal synthesis of TiO_2 particles; a $Ti(SO_4)_2$ solution was heated to 200°C or 400°C in the presence of hexaldehyde with the same condition as the TiO_2 colloid experiment. The XRD patterns of the precipitated particles indicated the formation of TiO_2 anatase phase (data not shown). Figure 2 shows the dispersibility of TiO_2 particles in dispersant. The bottles contain 0.42 g of modified TiO_2 in 6.0 ml iso-octane. Although the TiO_2 particles synthesized at 200°C were dispersed only in water phase (Figure 2a), the addition of hexaldehyde in the synthesis at 400°C resulted in a well dispersion of the synthesized particles in isooctane (shown in Figure 2b). This implies more efficient immobilization of hexaldehyde on the TiO_2 nanoparticles for the *in-situ* surface modification during the supercritical hydrothermal synthesis than for post surface modification.

In order to evaluate the binding strength of the organic molecules on the synthesized TiO_2 particles, TGA was performed (shown in Figure 3). The synthesized TiO_2 particles at 200°C in the presence of hexaldehyde showed the comparable

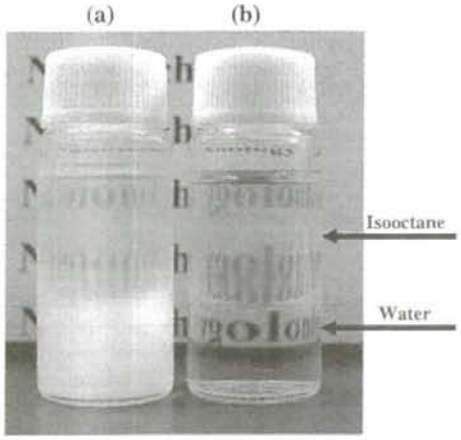

Figure 2. Dispersibility of TiO_2 nanoparticles synthesized with hexaldehyde: (a) at 200°C and (b) at 400°C, in a two-phase mixture of water and isooctane (ratio of hexaldehyde to aqueous solution is 38:1).

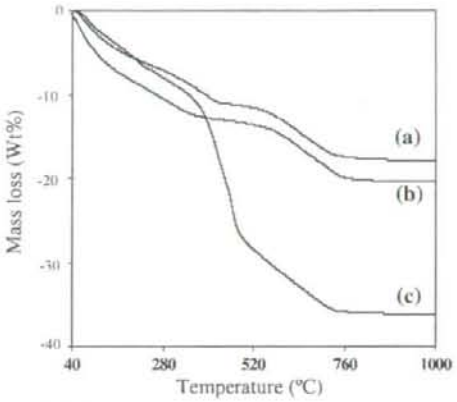

Figure 3. TGA curves of synthesized TiO_2 nanoparticles. (a) TiO_2 particles synthesized at 200°C without hexaldehyde; (b) TiO_2 particles synthesized at 200°C with hexaldehyde; (c) TiO_2 particles synthesized at 400°C with hexaldehyde.

TG curve to that of the synthesized TiO_2 particles without hexaldehyde. This result indicated that little amount of organic molecules bonded with the surface of nanoparticles. In contrast, the weight of the synthesized TiO_2 particles at 400°C with the organic molecules was drastically decreased around the 400°C. This supports the presence of organic compound only on the TiO_2 particles synthesized at 400°C. From the fact that the mass loss of the synthesized TiO_2 particles with the organic molecules was observed at high temperature, it is possible that the binding of the organic molecules on the TiO_2 particles is not physical adsorption, but rather, covalent binding. Density of organic molecule on the surface of nanoparticle was estimated from the specific surface area and the weight fraction of organic molecules on the particles. The specific surface area was estimated from the particle size (10 nm) observed by TEM, and the weight fraction was evaluated by TG analysis. Percentage of organic coverage (hexaldehyde) on the surface of nanoparticles synthesized at 400°C was evaluated to be about 70%. We analyzed the samples by FTIR and TGA for confirming the chemical bonding between organic modifier and particles surface (data not shown). FTIR analysis showed the presence of CH_2, CH_3 and C–O bonding as chemical bonds on the surface of TiO_2 nanoparticles, even after the several

times of the samples to remove physisorbed organic molecules. TGA (400°C) results showed the drastic decrease of the weight at above 300°C, which suggests decomposition of organic molecules. The physisorbed molecules which might not be washed out would be evaporated at a much lower temperature. From these two results, we concluded the chemical bonding between organic modifier and inorganic surface.

Although the detailed mechanism has not been elucidated, at the moment, we think a following reaction may occur: TiO_2 nuclei have been formed during hydrothermal synthesis, whose surface is hydroxide. When the organic species are added to the system, organic species and aqueous solution forms a homogeneous phase at the supercritical condition, and the organic molecules are chemisorbed or physisorbed on the surface of TiO_2 nuclei, which is followed by reaction (probably dehydration) to form chemical bonds.

Figure 4 shows the TEM images of the TiO_2 particles synthesized at 400°C. The synthesized TiO_2 particles without hexaldehyde used were aggregated and the size distribution was broad, ranging from several nm to 70 nm, while with the hexaldehyde, the particles were relatively dispersed on the grid and the size was in the range of several to 10 nm. It should be noted that the addition of the organic molecules resulted in the reduction of particle size and the dispersion of the particles. The immobilization of the organic molecules immediately after the nucleation of the particles probably suppressed the nuclei growth, and in addition, the formation of the organic layer also suppressed the aggregation of nanoparticles in the solution.

Supercritical hydrothermal reaction is one of the effective methods for the synthesis of highly-crystalline metal oxide materials. The high reaction rate of hydrothermal synthesis and low solubility of metal oxide in supercritical water result in the production of nanoparticles (Adschiri et al., 1992; Adschiri et al., 2001); however, nuclei growth is not completely controlled especially for the case of using a batch reactor where rapid heating of the solution cannot be achieved. Also, the perfect dispersion of the nanoparticles in an organic phase is difficult to achieve because of the high surface energy of the particles and the hydrophilic nature of the particles surface. The TiO_2 particles synthesized in this study, even by using batch reactor, were less than 10 nm in size and well dispersed in an organic phase. At the supercritical condition, the supercritical water forms a homogenous phase with organic molecules because of the lower dielectric constant of supercritical water, and dehydration occurs. Therefore, hexaldehyde might homogeneously and aggressively react with the metal hydrate, and thus, the particle growth is suppressed with a chemically bonded hydrophobic layer formed on its surface.

Conclusion

In conclusion, organic-ligand-assisted supercritical hydrothermal synthesis from $Ti(SO_4)_2$ and hexaldehyde can synthesize the organic-phase-dispersed

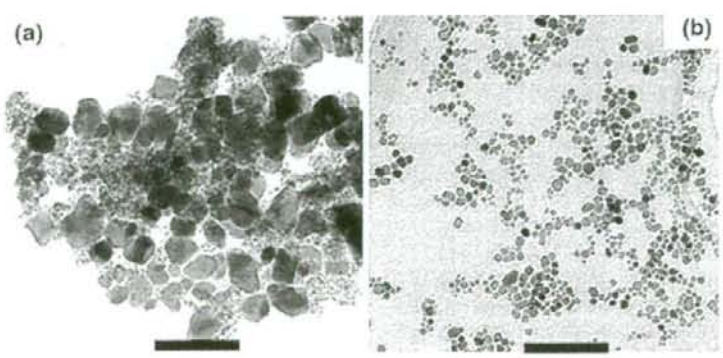

Figure 4. TEM images of TiO_2 nanoparticles synthesized at 400°C: (a) without hexaldehyde, (b) with hexaldehyde (Scale bar is 100 nm).

TiO_2 nanoparticles with chemically bonded organic molecules layer formed on their surfaces. The TEM images demonstrated that using the modifier reagent could control both the size and the aggregation of the nanoparticles; and size of nanocrystals synthesized at higher temperature was smaller. Besides, TG analysis confirmed high percentage of organic coverage on the nanoparticles surfaces synthesized at higher temperature, 400°C. The results of the dispersibility also revealed changing the surface property of the nanoparticles to hydrophobic. Therefore, the *in-situ* surface modification is very effective for making transparent dispersion in organic media. This noble synthesis method is expected to be applied for various combinations of metal oxides and organic modifiers.

Acknowledgments

This work was supported by a Scientific Research Grant from the Ministry of Education, Science, Sports, and Culture of Japan (T.A.). This research was also partly supported by the HEIWA NAKAJIMA foundation (T.A.) and by a Grant-in-Aid for the COE project, Giant Molecules and Complex Systems, 2002.

References

Adschiri T., K. Kanazawa & K. Arai, 1992. Rapid and continuous hydrothermal crystallization of metal-oxide particles in supercritical water. J. Am. Ceram. Soc. 75, 1019–1022.

Adschiri T., Y. Hakuta, K. Sue & K. Arai, 2001. Hydrothermal synthesis of metal oxide nanoparticles at supercritical conditions. J. Nanopart. Res. 3, 227–235.

Bonnemann H., G. Braun, W. Brijoux, R. Brinkmann, A.S. Tilling, K. Seevogel & K. Siepen, 1996. Nanoscale colloidal metals and alloys stabilized by solvents and surfactants – Preparation and use as catalyst precursors. J. Organomet. Chem. 520, 143–162.

Horn D. & J. Rieger, 2001. Organic nanoparticles in the aqueous phase – theory, experiment, and use. Angew. Chem. Int. Ed. 40, 4331–4361.

Li L.M., E. Beniash, E.R. Zubarev, W. Xiang, B.M. Rabatic, G. Zhang & S.I. Stupp, 2003. Assembling a lasing hybrid material with supramolecular polymers and nanocrystals. Nat. Mater. 2, 689–694.

Mousavand T., S. Takami, M. Umetsu, S. Ohara & T. Adschiri, 2006a. Supercritical hydrothermal synthesis of organic–inorganic hybrid nanoparticles. J. Mater. Sci. 41, 1445–1448.

Mousavand T., S. Ohara, M. Umetsu, J. Zhang, S. Takami, T. Naka & T. Adschiri, 2006b. Hydrothermal synthesis and in situ surface modification of boehmite nanoparticles in supercritical water. J. Supercritical Fluids. (accepted).

Sanchez C., G.J. De, F. Ribot, T. Lalot, C.R. Mayer & V. Cabuil, 2001. Designed hybrid organic–inorganic nanocomposites from functional nanobuilding blocks. Chem. Mater. 13, 3061–3083.

Singhal A., G. Skandan, A. Wang, N. Glumac, B.H. Kear & R.D. Hunt, 1999. On nanoparticle aggregation during vapor phase synthesis. Nanostruct. Mater. 11, 545–552.

ELSEVIER

Journal of Biomechanics 40 (2007) 2752–2757

JOURNAL OF BIOMECHANICS

www.elsevier.com/locate/jbiomech
www.JBiomech.com

In vitro confocal micro-PIV measurements of blood flow in a square microchannel: The effect of the haematocrit on instantaneous velocity profiles

Rui Lima[a,b,*], Shigeo Wada[c], Motohiro Takeda[a,d], Ken-ichi Tsubota[a], Takami Yamaguchi[a]

[a]*Department of Bioengineering and Robotics, Graduate School of Engineering, Tohoku University, 6-6-01 Aoba, 980-8579 Sendai, Japan*
[b]*Department of Mechanical Technology, ESTiG, Bragança Polytechnic Institute, Campus Sta. Apolónia, 5301-857 Bragança, Portugal*
[c]*Department of Mechanical Science and Bioengineering, Graduate School of Engineering Science, Osaka University, Toyonaka, 560-8531 Osaka, Japan*
[d]*Division of Surgical Oncology, Graduate School of Medicine, Tohoku University, 2-1 Seiryo-machi, Aoba-ku, 980-8575 Sendai, Japan*

Accepted 16 January 2007

Abstract

A confocal microparticle image velocimetry (micro-PIV) system was used to obtain detailed information on the velocity profiles for the flow of pure water (PW) and in vitro blood (haematocrit up to 17%) in a 100-μm-square microchannel. All the measurements were made in the middle plane of the microchannel at a constant flow rate and low Reynolds number ($Re = 0.025$). The averaged ensemble velocity profiles were found to be markedly parabolic for all the working fluids studied. When comparing the instantaneous velocity profiles of the three fluids, our results indicated that the profile shape depended on the haematocrit. Our confocal micro-PIV measurements demonstrate that the root mean square (RMS) values increase with the haematocrit implying that it is important to consider the information provided by the instantaneous velocity fields, even at low *Re*. The present study also examines the potential effect of the RBCs on the accuracy of the instantaneous velocity measurements.

Keywords: Microcirculation; Confocal micro-PIV; Instantaneous velocity profiles; Haematocrit; Red blood cells

1. Introduction

The velocity profiles of blood flow in vivo and in vitro have been measured using several techniques, including double-slit photometry (Gaehtgens et al., 1970; Baker and Wayland, 1974), video microscopy and image analysis (Bugliarello and Hayden, 1963; Tangelder et al., 1986; Parthasarathi et al., 1999), laser-Doppler anemometry (Einav et al., 1975; Born et al., 1978; Cochrane et al., 1981; Uijttewaal et al., 1994, Golster et al., 1999), and particle-measuring methods (Sugii et al., 2002, 2005; Nakano et al., 2003, 2005; Jeong et al., 2007). Nevertheless, no general consensus yet exists concerning the actual velocity profile in microvessels. While some studies have reported parabolic profiles (Baker and Wayland, 1974; Golster et al., 1999; Sugii et al., 2005), others have suggested blunt profiles (Bugliarello and Hayden, 1963; Tangelder et al., 1986; Nakano et al., 2003); still others have reported blunt profiles at extremely low velocities and diameters and parabolic profiles at diameters exceeding 100 μm (Gaehtgens et al., 1970; Cochrane et al., 1981). Thus, further research is needed on the influence of flow parameters on the blood flow velocity profiles in microvessels.

Due to its outstanding spatial filtering technique and multiple point light illumination system, confocal microparticle image velocimetry (micro-PIV) (Tanaani et al., 2002; Park et al., 2004; Kinoshita et al., 2005; Park and Kihm, 2006; Lima et al., 2006a) has become accepted as a reliable method for measuring velocity profiles with high spatial resolution. Very recently, we demonstrated the ability of confocal micro-PIV to measure both homogeneous and nonhomogeneous fluids (Lima et al., 2006a).

*Corresponding author. Tel.: +81 22 7956958; fax: +81 22 7956959.
E-mail address: rui@pfsl.mech.tohoku.ac.jp (R. Lima).

0021-9290/$ - see front matter © 2007 Elsevier Ltd. All rights reserved.
doi:10.1016/j.jbiomech.2007.01.012

The present study compared the instantaneous and ensemble velocities profiles of pure water and blood flow in vitro. The velocity profiles of both pure water and in vitro blood with two different haematocrits (9 and 17% Hct) were acquired in the centre plane of a 100-μm square microchannel.

2. Materials and methods

2.1. Working fluids and microchannel

This study examined three working fluids: pure water (PW) and physiological saline (PS) containing 9% (9 Hct) or 17% (17 Hct) human red blood cells (RBCs). All the fluids were seeded with 0.15% (by volume) 1-μm-diameter red fluorescent solid polymer microspheres (R0100; Duke Scientific, Palo Alto, CA, USA). The blood used was collected from a healthy adult volunteer, and ethylenediaminetetraacetic acid (EDTA) was added to prevent coagulation. The RBCs were separated from the bulk blood by centrifugation (1500 rpm for 20 min) and the plasma and buffy coat were removed by aspiration. The washing and centrifuging with PS was repeated twice. The remaining RBCs were then resuspended in PS to make up the required RBC concentration by volume. The haematocrit of the two RBC suspensions used in this study was about 9% (9 Hct) and 17% (17 Hct), respectively. All the blood samples were stored hermetically at 4 °C until the experiment was performed at room temperature (25–27 °C).

In this study, we used a 100-μm-square borosilicate glass microchannel fabricated by Vitrocom (Mountain Lakes, NJ, USA), which was mounted on a glass slide immersed in glycerol that had the same refractive index. A square microchannel was selected to minimise possible refraction of the laser beam at the walls of the microchannel. Using a glass tube, the refraction arising from the curved walls would be more pronounced and might degrade the measured velocity fields.

2.2. Experimental setup

The confocal micro-PIV system we used consisted of an inverted microscope (IX71; Olympus, Tokyo, Japan) combined with a confocal scanning unit (CSU22; Yokogawa Corporation, Tokyo, Japan) and a diode-pumped solid-state (DPSS) continuous wave (CW) laser (Laser Quantum, Stockport, UK) with an excitation wavelength of 532 nm. A high-speed camera (Phantom v7.1; Vision Research, Wayne, NJ, USA) was connected to the outlet port of the CSU22. The microchannel was placed on the stage of an inverted microscope and the flow rate (Q) of the working fluids was kept constant at 0.15 μl/min using a syringe pump (KD Scientific, Holliston, MA, USA), corresponding to a Reynolds number (Re) of 0.025.

The laser beam was illuminated from below the microscope stage through a 20 × objective dry lens with a numerical aperture (NA) equal to 0.75. Satisfactory illumination was achieved by seeding 1-μm-diameter fluorescent particles that absorb green light (absorbance peak 542 nm) and emit red light (emission peak 612 nm). The light emitted from the fluorescent flowing particles passes through a colour filter into the CSU22 scanning unit, where it is reflected onto a high-speed camera using a dichromatic mirror to record the PIV images.

In order to obtain adequate quality images for processing with the PIV software (PivView; PivTec GmbH, Göttingen, Germany), we captured images with a resolution of 640 × 480 pixels and 12-bit greyscale, at a rate of 200 frames/s, with an exposure time of 4995 μs, and a time interval (Δt) of 5 and 10 ms between two images. All the PIV measurements were performed for a period of approximately 0.5 s in order to obtain both instantaneous and ensemble averaged velocities. After recording the images, they were digitised and transferred to a computer for evaluation using Phantom camera control software (PH607). The PIV images of the flowing particles were processed and the flow velocity was determined using PivView version 2.3 (Raffel et al., 1998). The images were evaluated using a cross-correlation method in which the time between two images was set to 5 and 10 ms for all working fluids. Using a multiple-pass interrogation algorithm with a 24 × 16 pixel interrogation window (50% overlap), which corresponds to a spatial resolution of 28.24 × 18.83 μm, it was possible to obtain the corresponding instantaneous and ensemble velocity fields. A full description and evaluation of the confocal micro-PIV system used in this study can be found in Lima et al. (2006a).

3. Results and discussion

3.1. Ensemble velocity profiles

Most previous studies have determined the velocity profiles of flowing blood by measuring the time-averaged velocity field. Fig. 1(a) and (b) shows the averaged velocity of 100 ($\Delta t = 5$ ms) and 50 ($\Delta t = 10$ ms) ensemble PIV images, respectively. These images were recorded at the same time period of approximately 0.5 s. Fig. 1 also compares the PIV measurements with an analytical solution for steady flow through a long, straight, rigid square microchannel (see Lima et al., 2006a for more details).

Comparing the ensemble velocity profiles of all fluids (see Fig. 1), we observed small deviations (<5%) for both $\Delta t = 5$ and 10 ms, especially in the central region of the velocity profile. Using the t-test analysis we found no significant difference between the working fluids and the analytical solution at 98% confidence interval. Hence, these results imply that the ensemble-averaged velocity profiles of in vitro blood with haematocrits up to 17% flowing within a 100-μm square microchannel do not change significantly from a parabolic shape. These results agree with Baker and Wayland (1974) and Sugii et al. (2005). Furthermore, from the ensemble-averaged velocity profiles for both $\Delta t = 5$ and 10 ms the average deviation was estimated to be 2% for PW and 17% Hct and 5% for 9% Hct. On comparing the results from both Δt we found no significant difference between $\Delta t = 5$ and 10 ms at 98% confidence interval. These results suggest that for both cases it is possible to obtain reliable ensemble-averaged velocity profiles for all the working fluids used in this study.

3.2. Instantaneous velocity profiles and root mean square (RMS)

A remarkable advantage of the PIV measuring technique over conventional methods, such as double-slit photometry or laser–Doppler anemometry, is its ability to obtain detailed information on the fluid flow behaviour from the evaluation of the instantaneous velocity fields. Although these velocity fields are extremely important for flows with high Re in which turbulent flow fields are likely to occur (Meinhart et al., 2000a; Bates et al., 2001; Heise et al., 2004), we believe that instantaneous velocities are also crucial for evaluating several phenomena in steady flows, especially for complex fluids containing suspended blood cells in plasma. In this way, Figs. 2–4 show the first time series of the instantaneous velocity profiles of pure water